Chemical Science

ROYAL SOCIETY OF CHEMISTRY

EDGE ARTICLE

View Article Online
View Journal | View Issue

Cite this: *Chem. Sci.*, 2024, **15**, 18455

All publication charges for this article have been paid for by the Royal Society of Chemistry

A three-dimensional lead iodide perovskite analog featuring hydrogen-bonded dual monovalent cations†

Wei Wang, Cheng-Dong Liu, Chang-Chun Fan and Wen Zhang *

Received 20th August 2024
Accepted 11th October 2024

DOI: 10.1039/d4sc05585c

rsc.li/chemical-science

Three-dimensional (3D) halide perovskites have attracted considerable research interest, yet the selection of A-site cations is restricted by the Goldschmidt tolerance factor. To accommodate cations beyond this acceptable range, novel 3D perovskite analog structures with edge- and face-sharing motifs have been developed. Until now, these structures have been limited to divalent cations due to significant electrostatic repulsion when incorporating two monovalent cations. Herein, we employ a supramolecular synthon mechanism to address the issue and an effective hydrogen-bonding pattern is achieved in a novel 3D lead iodide hybrid perovskite, (ammonium)(morpholinium)Pb_2I_6 (**1**). The inorganic framework of **1** consists of two edge-shared [PbI_6] octahedra connected *via* corner-sharing, thus forming a continuous 3D network. Structural analysis indicates that the spatial separation of N atoms and the existence of N–H···O hydrogen bonds effectively eliminate electrostatic repulsion. This work has demonstrated the potential to mitigate constraints of cation selection on 3D frameworks and could spur the development of novel 3D perovskite materials and related fields.

Introduction

Halide perovskites (HPs) have attracted significant attention due to their remarkable properties, including ferroelectricity,[1,2] piezoelectricity,[3,4] photoluminescence,[5] and their applications in photodetection and photovoltaics.[6–11] Among them, three-dimensional (3D) HPs are extensively studied for their high absorption coefficients,[12] high defect tolerance,[13] long carrier diffusion lengths,[14–16] and cost-effective solution processing.[17] These characteristics have accelerated advancements in technologies such as solar cells,[18] light-emitting diodes,[19] photodetectors,[20] and lasers.[21] Typically represented by the general formula AMX_3 (Fig. 1a), where A is a monovalent cation, M is a divalent metal, and X is a halide, the phase stability of the 3D perovskites are influenced by the Goldschmidt tolerance factor $t = (r_A + r_X)/[\sqrt{2}(r_M + r_X)]$, where r_A, r_M, and r_X denote the effective ionic radii.[22–24] Perovskite phases typically form effectively when $0.8 < t < 1$, with deviations often resulting in non-perovskite structures. Consequently, the choice of A-site cations is restricted to small sizes. Currently, only a few monovalent cations, *i.e.*, Cs^+, $CH_3NH_3^+$, $CH_3NH_2NH_2^+$, $HC(NH_2)_2^+$ and aziridinium, have been identified as capable of maintaining the typical conner-shared 3D perovskite structure.[25–29] Attempts to incorporate larger cations generally lead to lower-dimensional structures that hinder charge transport in at least one direction.[30–32]

Recently, novel 3D perovskite analogs have emerged that can accommodate large diammonium cations.[33–41] The fundamental building blocks consist of edge-shared [M_2X_{10}] units which further link through corner-sharing to form 3D frameworks capable of hosting divalent cations within either parallelepiped-shaped (Type I) or trigonal prism-shaped (Type II) voids (Fig. 1b and c). Synthetically, symmetric cations typically lead to type I voids[39] while less symmetric ones result in type II.[38,40] In essence, these 3D perovskite analogs are composed of edge-sharing octahedral dimers, with voids large enough to accommodate either two monovalent cations ($A_2M_2X_6$) or one divalent cation ($A'M_2X_6$). The resulting chemical formulas, $A_2M_2X_6$ or $A'M_2X_6$, effectively double the unit cell compared to traditional 3D perovskites. However, the reported structures are presently exclusively limited to $A'M_2X_6$ because the presence of significant electrostatic repulsion between two positively charged monocations within the void could make $A_2M_2X_6$ energetically unfavorable and synthetically difficult. Considering the much higher abundance of monocations than dications, it is necessary to overcome this challenge to enrich the 3D perovskite family.

Herein, we employ a supramolecular synthon mechanism to address the issue caused by electrostatic repulsion of two positively charged monocations (Fig. 1d). Through carefully selecting the monocation pair, an effective hydrogen-bonding

Jiangsu Key Laboratory for Science and Applications of Molecular Ferroelectrics, School of Chemistry and Chemical Engineering, Southeast University, Nanjing 211189, China. E-mail: zhangwen@seu.edu.cn

† Electronic supplementary information (ESI) available: Experimental details, Fig. S1–S9 and Tables S1–S5. CCDC 2387432. For ESI and crystallographic data in CIF or other electronic format see DOI: https://doi.org/10.1039/d4sc05585c

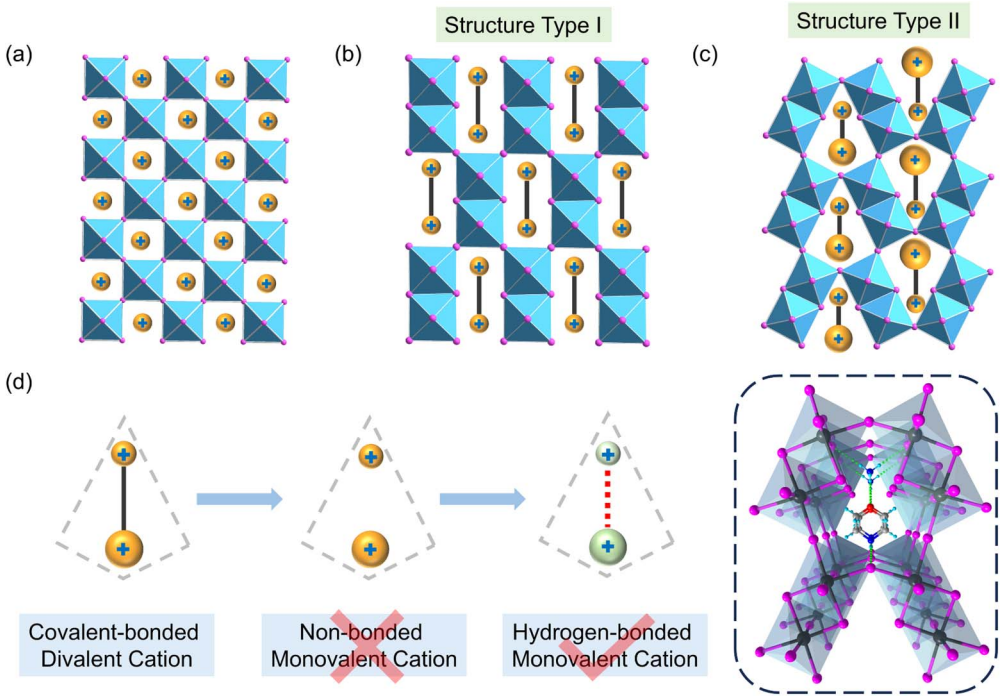

Fig. 1 Octahedra connecting types of reported 3D perovskites: (a) classical AMX_3; (b) type I; (c) type II. (d) Type II 3D perovskite analog with hydrogen-bonded monovalent cations reported in this work.

pattern is achieved between them to result in a pseudo-divalent cation and thus favor the formation of the type II framework. A synthesized model 3D perovskite analog (ammonium)(morpholinium)Pb_2I_6 (**1**) shows that the ammonium and morpholinium cations occupy the smaller and larger part of the void, respectively, based on their volumes. Structure analysis clarifies that the remote relative position of two positively charged N atoms and intermolecular N–H···O hydrogen bonding interaction helps to diminish the electrostatic repulsion. Compound **1** has an indirect bandgap, akin to the electronic band patterns found in AMX_3 perovskites, featuring notably dispersive valence and conduction bands. And it also exhibits a good photoelectric response, thermal stability up to 250 °C and excellent long-term stability under conditions of 40% relative humidity. This work shows promise in overcoming limitations related to cation selection in 3D frameworks and may inspire the creation of new 3D perovskite materials.

Results and discussion

Synthesis

Compound **1** was synthesized using a solution-based method. In contrast to previously reported type I and type II 3D perovskite analogs, which require an excess of PbI_2 to prevent the formation of other phases, **1** was synthesized with a ratio of NH_4I : morpholine : PbI_2 = 2 : 1 : 1. The solution was heated to over 110 °C and then gradually cooled to 90 °C, leading to the precipitation of red crystals within 12 hours (Fig. 2a). More details about crystal synthesis are provided in the ESI.† Phase purity of the sample was verified by powder X-ray diffraction (PXRD) by comparing experimental and simulated diffraction patterns (Fig. S1†).

Crystal structure analysis

Single-crystal diffraction analysis of **1** reveals a monoclinic structure within the $P2_1/m$ space group, characterized by cell parameters of $a = 6.3366(3)$ Å, $b = 16.1613(7)$ Å, $c = 10.1821(4)$ Å, $\alpha = 90°$, $\beta = 93.579(4)°$, $\gamma = 90°$, and volume $V = 1040.69(8)$ Å^3 (Table S1†). The structure features inorganic dimers composed of two edge-sharing octahedra of adjacent Pb ions. Four dimers, connected *via* corner-sharing, constitute a trigonal prism-shaped void (Fig. 2b). Further corner-sharing of these dimers extends in *bc* plane to form a continuous inorganic layer and the layers are stacked along the *a*-axis by angle-to-angle connections to result in a 3D inorganic framework (Fig. 2c and d), as classified as type II 3D perovskite. This unique arrangement of the inorganic framework provides ample space to accommodate two monovalent cations, which are anchored to the halide ions of PbI_6 octahedra through N–H···I hydrogen bonding interactions (Fig. 2e, f, Tables S2 and S3†). Specifically, within the trigonal prism-shaped void, the NH_4^+ and morpholinium cations occupy the smaller and larger volume sides, respectively, reflecting their significant volume disparity. Regarding the structure, positively charged N atoms of NH_4 and morpholinium cations are strategically positioned on opposite sides of the void, thereby minimizing electrostatic repulsion. Meanwhile, the N–H···O hydrogen bonding interactions between the NH_4^+ and morpholinium cations further reduce electrostatic repulsion and enhance structural stability. This marks the first successful filling of a void in a 3D perovskite analog structure with mixed

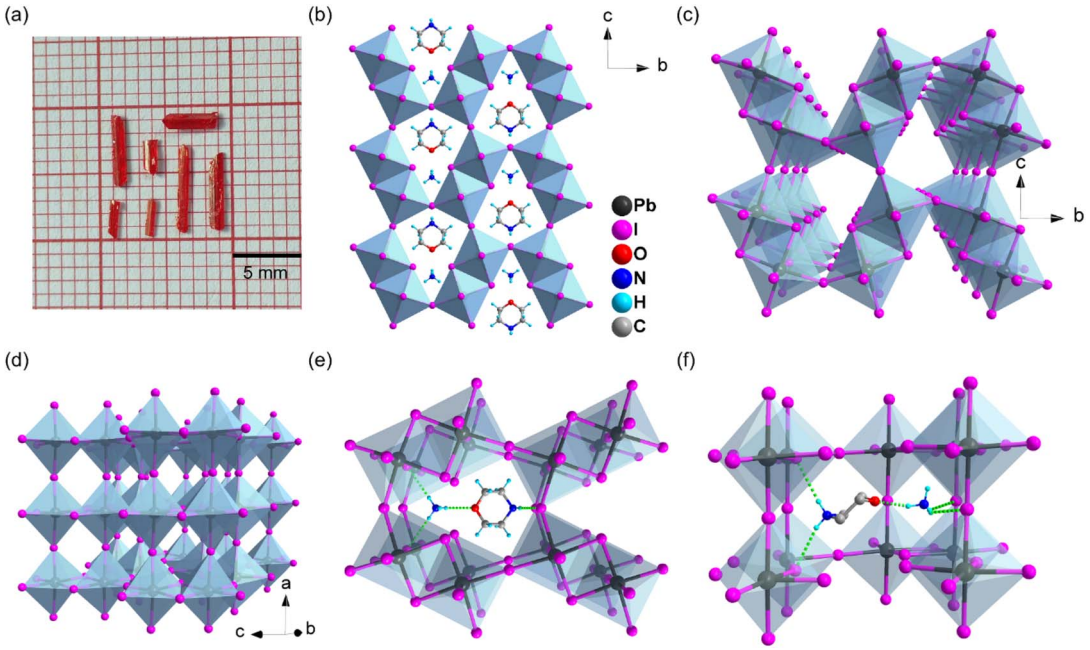

Fig. 2 (a) Crystal image of **1**. (b) basic structure motif of **1** viewed from *a* direction. (c and d) Inorganic framework showing 3D connectivity. Organic parts are omitted for clarity. (e and f) Hydrogen bonding interactions within and between the organic parts and inorganic framework.

monovalent cations *via* intermolecular hydrogen bonds to overcome the electrostatic repulsion between positively charged species.

Given the flexibility of monocations, we aim to identify other cations that could potentially replace morpholinium to form similar 3D frameworks. We selected several cations for calculation based on their comparable volumes and shapes, as well as their potential to form hydrogen bonds with NH_4^+. According to Table S4,† our calculations suggest that thiomorpholinium, 4-hydroxypiperidinium, and tetrahydro-2*H*-pyran-4-aminium are promising candidates, with volume differences of less than 5%. However, experimental validation is further required to confirm these findings.

Because of the strong links to the electronic properties, it is important to analyze the connectivity types of the metal iodide octahedra in the structure as well as the M–X–M angles and bond distortions. To simplify the discussion, we measure the Pb–I–Pb angles by taking the two edge-shared octahedra as a whole basic unit and only consider the Pb–I–Pb angles of corner-sharing connectivity since they are the special feature in perovskites and most relevant to the charge transport and electronic band dispersion. As shown in Fig. 3, **1** has three different Pb–I–Pb angles. The largest one is 180°, which is slightly higher than that of $(TMEA)Pb_2Br_6$ (Fig. S2,† TMEA = *N*,*N*,*N*-trimethylethane-1,2-diaminium),[35] indicating the structure is not tilted and very similar to type II structure. In the *a* axial direction where the octahedra are connected by corner-sharing, the Pb–I–Pb angles are 173.61°, closely to 180°. The smallest one is 146.16°, much smaller than 180°. The average Pb–I–Pb angle is calculated to be 166.59°, showing slightly smaller than that of $(TMEA)Pb_2Br_6$.

We also assess the distortion levels of individual octahedra by using the distortion index (Δd) and bond angle variance (σ^2), which are defined based on the variations in Pb–I bond lengths and Pb–I–Pb bond angles as shown in eqn (1) and (2):

$$\Delta d = \left(\frac{1}{6}\right)\sum_{i=1}^{6}\left(\frac{d_i - d}{d}\right)^2 \quad (1)$$

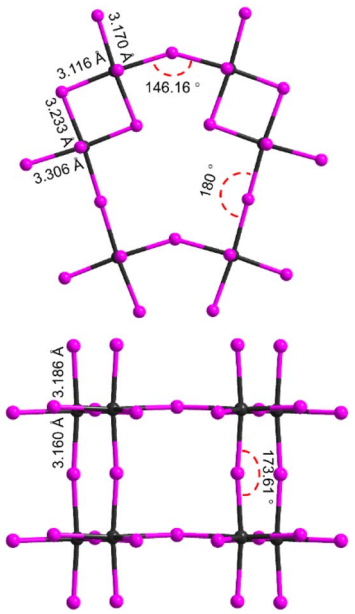

Fig. 3 Summary of bond angles between inter-dimer Pb–I–Pb bonds and bond lengths within each octahedron.

$$\sigma^2 = \left(\frac{1}{11}\right)\sum_{i=1}^{12}(\theta_i - 90)^2 \quad (2)$$

where d and d_i are the average and individual bond distance, respectively, and θ_i is the individual angle. For **1**, the two octahedra forming the dimer exhibit similar levels of distortion with Δd and σ^2 of 3.58×10^{-4} and 12.48, respectively. The values are notably lower than those typically reported for 3D edge-shared HPs,[35,41] suggesting a minimal distortion close resemblance to an ideal structural model.

Electronic band structure

Density functional theory (DFT) calculations were conducted to analyze the electronic band structures and dimensional properties of **1**. As depicted in Fig. 4a, the valence band maximum (VBM) appears at the A point while the conduction band minimum (CBM) lies at the Y_2 point. The calculated band structure reveals an indirect feature with a bandgap of 1.86 eV, which exceeds that of corner-sharing $MAPbI_3$ (1.5 eV) and is comparable to 3D lead iodide hybrid perovskite analogs with similar edge-sharing dimers (*e.g.*, 1.93 eV of $(M_2pda)Pb_2I_6$ (M_2pda = *N*,*N*′-dimethylpropane-1,3-diaminium)).[36] Compound **1** exhibits relatively flat valence bands and dispersive conduction bands. This is because the octahedra are connected in a corner-sharing mode along *a* direction while a combination of corner-sharing and edge-sharing is observed in the other two directions. Consequently, the Γ-Y_2 direction in the Brillouin zone, corresponding to *a* direction in real space, exhibits the most energy dispersion for conduction bands. This contrasts sharply with other crystallographic directions where octahedra share edges, resulting in significantly less dispersive electronic bands. This is also evident from the calculated effective masses (Table S5†). The effective mass for both electrons and holes along *a* direction is significantly smaller than in the other two directions, indicating that charge transport is greatly restricted in the edge-sharing plane.[35,41] These results align with our understanding that the corner-shared motif generally results in greater band dispersions compared to the edge-shared one, followed by the face-shared motif.[42–44]

Density of states data indicates that the VBM is formed by overlapping Pb-6s and I-5p orbitals while the CBM results from overlapping Pb-6p orbitals, highlighting that the energy band and semiconductor performance are predominantly governed by the inorganic components, with negligible contributions from organic cations (Fig. 4b). Additionally, partial charge density (PCD) distributions of the CBM and VBM were computed to deepen the understanding of the electronic properties. Analysis of the charge density associated with the VBM and CBM in the *bc* plane also reveals that the VBM is primarily contributed by Pb and I whereas Pb dominates in the CBM (Fig. 4c and d). Contour plots of the PCD for the CBM and VBM within the *bc* plane demonstrate directional differences along the *b* and *c* axes, indicating anisotropic electronic characteristics. Nevertheless, the orbitals contributing to the VBM and CBM maintain continuity across all three crystallographic axes (Fig. S3†). Owing to the 3D connectivity of the band edge-determining $[PbI_6]$ octahedra, **1** showcases a 3D electronic nature, which aligns with the structural connectivity of its inorganic framework.

Optical properties

Ultraviolet-visible diffuse-reflectance spectra of **1** were recorded and shown in Fig. 5a. There is significant absorption in the ultraviolet region. The edge of the band extends into the visible light region near 600 nm. Based on the Kubelka–Munk equation,[45] the optical bandgap value is estimated to be 2.10 eV (Fig. 5a inset), which is slightly smaller than the bandgap of common 2D lead iodide perovskite semiconductors[42] and is

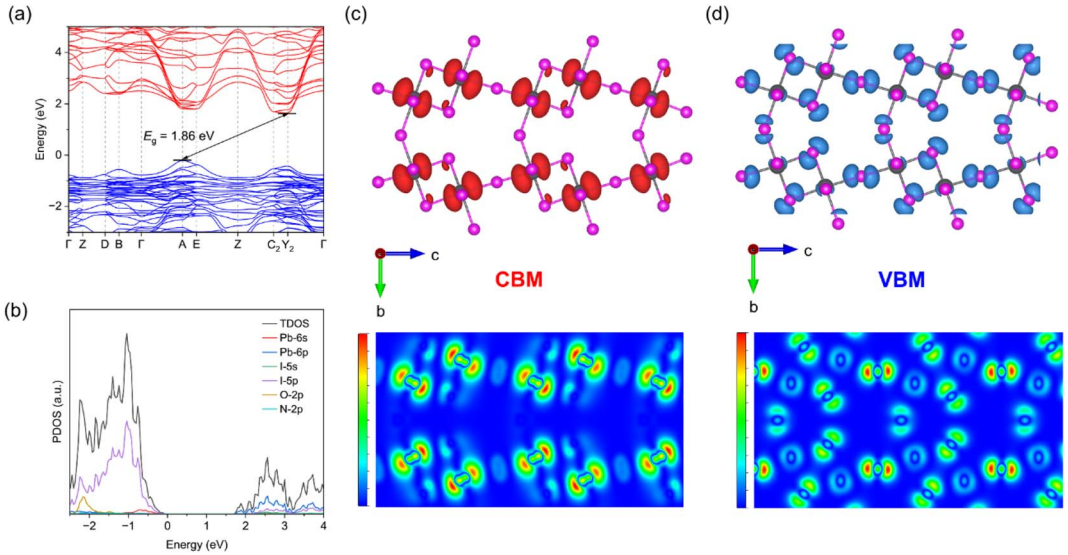

Fig. 4 DFT calculations of the electronic structural features of **1**: (a) band structures and (b) projected density of states (DOS); calculated partial charge densities (PCD) and 2D maps within the (100) plane for (c) VBM and (d) CBM.

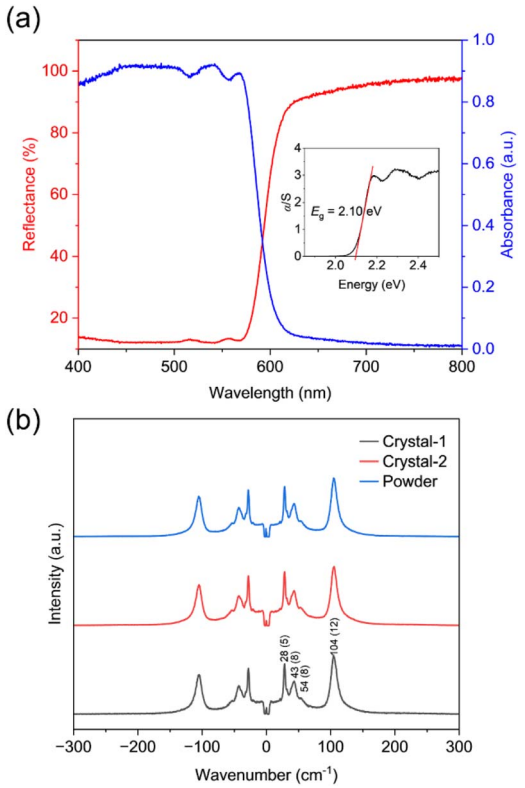

Fig. 5 (a) UV-visible diffuse-reflectance spectra and (b) low-frequency Raman spectra of **1**. The full-width at half-maximum (FWHM) indicated in parentheses.

comparable to 3D lead iodide perovskite $(M_2pda)Pb_2I_6$.[36] A steady-state photoluminescence (PL) spectrum of the powder sample of compound **1** was recorded with 460 nm excitation. At room temperature, **1** exhibits weak emission, similar to many 3D lead perovskite analogs.[35,41] The PL spectrum reveals a relatively narrow peak at 590 nm with a full width at half maximum (FWHM) of approximately 40 nm (Fig. S4a†). This contrasts with previously reported results for $(NMPA)Pb_2Br_6$ (NMPA = *N*,*N*′-dimethylpropane-1,3-diaminium) and $(DMEA)Pb_2Br_6$ (DMEA = *N*,*N*-dimethylethane-1,2-diaminium), which display broader emission.[35] And the extracted PL lifetime by fitting the PL decay curves demonstrate a short lifetime of 0.74 ns (Fig. S4b†). Combining with the fact that the emission peak is near the band edge, the PL emission of **1** is likely to be excitonic. However, additional experimental evidence, such as temperature-dependent and power-dependent PL measurements, would be helpful.

Raman spectroscopy of **1** was performed at room temperature to explore the dynamic characteristics (Fig. 5b). It exhibits obvious peaks at 28, 43, and 104 cm^{-1}, similar to those observed in conventional 3D AMX_3 structures. Notably, peaks around 105 cm^{-1} are assigned to the symmetric and asymmetric stretching of $[PbI_6]$ octahedra while those below 85 cm^{-1} correspond to octahedral bending modes.[41,46] The FWHM of these peaks are relatively narrow,[47–49] indicating the absence of disorder at room temperature, which was in agreement with X-ray diffraction result. The Fourier transform infrared (FT-IR) spectroscopy was conducted to investigate the interaction between the organic molecules and the inorganic framework. The signals around 3570, 3500 and 3130 cm^{-1}, attributed to N–H vibration of **1**, shift to higher wavenumbers compared to that of the precursor cations, indicating the presence of weak hydrogen bonding interactions between the organic molecular cations and the $[PbI_6]$ octahedral frameworks (Fig. S5†). And these signals are sharp than the observed broad peak in NH_4I precursor, which may indicate an order of NH_4^+ in the lattice. Theses observation aligns with the structural analysis described above.

Optoelectronic response

Based on the promising optical and electronic properties of **1**, we conducted an initial evaluation of its photoresponse characteristics. Silver electrodes were utilized with the direction oriented along the *a*-axis, where all the octahedra are interconnected by corner-sharing. When subjected to ambient light at a wavelength of 565 nm, the device exhibited a distinct photoresponse, even under low power conditions of 1.6 μW cm^{-2} (Fig. S6a†). The on-off photoresponse increased with the power of the light, and at a light power of 62.9 μW cm^{-2}, the device demonstrated a pronounced photoresponse with a photocurrent that was 10 times higher than the dark current. Furthermore, stability and durability tests under pulsed light revealed that the device maintained excellent photoelectric performance even after more than 10^3 cycles (Fig. S6b†). These findings indicate significant potential for photodetection applications at room temperature.

Structural phase transition and stability

In the context of known 3D perovskites or analogs, many exhibit structural phase transitions.[33,36] However, in the case of **1**, differential scanning calorimetry measurements indicate no phase transition within the measured temperature range (Fig. S7a†). The temperature-dependent dielectric measurements show no anomalies during heating and cooling, which aligns with the DSC results, further confirming that there is no structural phase transition (Fig. S7b†). Thermogravimetric analysis (TGA) evaluated the thermal stability of **1**, demonstrating a good stability up to approximately 250 °C (Fig. S8†). This stability, while slightly lower than 3D perovskites containing dications, is attributed to the lighter NH_4^+ and weak N–H···O interactions. Furthermore, after exposure to 40% relative humidity for three months, the powders of **1** maintained a consistent PXRD pattern with fresh one, highlighting its good long-term stability (Fig. S9†).

Conclusions

In summary, we successfully synthesized a 3D perovskite analogue, (ammonium)(morpholinium)Pb_2I_6, by strategically replacing one dication with two hydrogen-bonded monocations in the voids. This innovative approach effectively mitigates issues stemming from electrostatic repulsion between two positively charged monocations. The fundamental 3D inorganic

framework adopts a type II structure with minimal structural distortion, accommodating ammonium and morpholinium cations in regions of varying volume based on their respective sizes. Detailed structural analysis reveals that the spatial arrangement of the two positively charged nitrogen atoms and the N–H···O hydrogen bonding interactions play a crucial role in reducing electrostatic repulsion. Density functional theory calculations indicate that **1** exhibits an indirect bandgap, similar to the electronic band structures observed in AMX_3 perovskites, with relatively dispersive valence and conduction bands. The synthesis of such a 3D perovskite holds promise for alleviating limitations in cation selection and has the potential to catalyze the developments of new 3D perovskite materials and related fields.

Data availability

The data supporting this article have been included as part of the ESI.†

Author contributions

Wei Wang: conceptualization, data curation, formal analysis, investigation, methodology, validation and writing original draft; Cheng-Dong Liu: visualization and formal analysis; Chang-Chun Fan: investigation; Wen Zhang: conceptualization, data curation, funding acquisition, resources, supervision, software and writing – review & editing.

Conflicts of interest

The authors declare no competing financial interest.

Acknowledgements

This work was financially supported by the National Natural Science Foundation of China (21991144 and 22475040). We thank the Big Data Computing Center of Southeast University for providing facility support for the calculations.

References

1 C. C. Fan, X. B. Han, B. D. Liang, C. Shi, L. P. Miao, C. Y. Chai, C. D. Liu, Q. Ye and W. Zhang, Chiral Rashba Ferroelectrics for Circularly Polarized Light Detection, *Adv. Mater.*, 2022, **34**, e2204119.

2 C. D. Liu, C. C. Fan, B. D. Liang, C. Y. Chai, C. Q. Jing, X. B. Han and W. Zhang, Spectrally Selective Polarization-Sensitive Photodetection Based on a 1D Lead-Free Hybrid Perovskite Ferroelectric, *ACS Mater. Lett.*, 2023, **5**, 1974–1981.

3 P. Chen, C. Cheng, X. Yang, T. T. Sha, X. Zou, F. Zhang, W. Jiang, Y. Xu, X. Cao, Y. M. You and Z. Luo, Wireless Deep Brain Stimulation by Ultrasound-Responsive Molecular Piezoelectric Nanogenerators, *ACS Nano*, 2023, **17**, 25625–25637.

4 T. M. Guo, F. F. Gao, Y. J. Gong, Z. G. Li, F. Wei, W. Li and X. H. Bu, Chiral Two-Dimensional Hybrid Organic-Inorganic Perovskites for Piezoelectric Ultrasound Detection, *J. Am. Chem. Soc.*, 2023, **145**, 22475–22482.

5 W. Wang, C.-D. Liu, X.-B. Han, C.-Q. Jing, C.-Y. Chai, C.-C. Fan, M.-L. Jin, J.-M. Zhang and W. Zhang, Photoluminescence Switching and Non-Volatile Memory in Hybrid Metal-Halide Phase-Change Materials, *ACS Mater. Lett.*, 2024, **6**, 203–211.

6 J. Huang, Y. Yuan, Y. Shao and Y. Yan, Understanding the physical properties of hybrid perovskites for photovoltaic applications, *Nat. Rev. Mater.*, 2017, **2**, 19.

7 J. V. Passarelli, D. J. Fairfield, N. A. Sather, M. P. Hendricks, H. Sai, C. L. Stern and S. I. Stupp, Enhanced Out-of-Plane Conductivity and Photovoltaic Performance in n = 1 Layered Perovskites through Organic Cation Design, *J. Am. Chem. Soc.*, 2018, **140**, 7313–7323.

8 W. Wang, C. D. Liu, C. C. Fan, X. B. Fu, C. Q. Jing, M. L. Jin, Y. M. You and W. Zhang, Rational Design of 2D Metal Halide Perovskites with Low Congruent Melting Temperature and Large Melt-Processable Window, *J. Am. Chem. Soc.*, 2024, **146**, 9272–9284.

9 C. D. Liu, C. C. Fan, B. D. Liang and W. Zhang, A polar two-dimensional lead-free hybrid perovskite for self-powered polarization-sensitive photodetection, *Inorg. Chem. Front.*, 2024, **11**, 4611–4618.

10 B.-D. Liang, C.-C. Fan, C.-D. Liu, T.-Y. Ju, C.-Y. Chai, X.-B. Han and W. Zhang, Large in-plane anisotropic 2D perovskites toward highly linear polarized light responses, *Inorg. Chem. Front.*, 2023, **10**, 5035–5043.

11 C. D. Liu, C. C. Fan, B. D. Liang, W. Wang, M. L. Jin, C. Q. Jing, J. M. Zhang and W. Zhang, Quantum well thickness control of a hybrid perovskite to achieve a tunable anisotropic photoresponse, *J. Mater. Chem. C*, 2024, **12**, 12734–12738.

12 M. A. Green, Y. Jiang, A. M. Soufiani and A. Ho-Baillie, Optical Properties of Photovoltaic Organic–Inorganic Lead Halide Perovskites, *J. Phys. Chem. Lett.*, 2015, **6**, 4774–4785.

13 J. Kang and L.-W. Wang, High Defect Tolerance in Lead Halide Perovskite $CsPbBr_3$, *J. Phys. Chem. Lett.*, 2017, **8**, 489–493.

14 S. D. Stranks, G. E. Eperon, G. Grancini, C. Menelaou, M. J. P. Alcocer, T. Leijtens, L. M. Herz, A. Petrozza and H. J. Snaith, Electron-Hole Diffusion Lengths Exceeding 1 Micrometer in an Organometal Trihalide Perovskite Absorber, *Science*, 2013, **342**, 341–344.

15 D. Shi, V. Adinolfi, R. Comin, M. Yuan, E. Alarousu, A. Buin, Y. Chen, S. Hoogland, A. Rothenberger, K. Katsiev, Y. Losovyj, X. Zhang, P. A. Dowben, O. F. Mohammed, E. H. Sargent and O. M. Bakr, Low trap-state density and long carrier diffusion in organolead trihalide perovskite single crystals, *Science*, 2015, **347**, 519–522.

16 G. Long, Y. Zhou, M. Zhang, R. Sabatini, A. Rasmita, L. Huang, G. Lakhwani and W. Gao, Theoretical Prediction of Chiral 3D Hybrid Organic-Inorganic Perovskites, *Adv. Mater.*, 2019, **31**, e1807628.

17 Z. Saki, M. M. Byranvand, N. Taghavinia, M. Kedia and M. Saliba, Solution-processed perovskite thin-films: the

journey from lab- to large-scale solar cells, *Energy Environ. Sci.*, 2021, **14**, 5690–5722.

18 H. J. Zhang, Z. J. Shi, L. G. Hu, Y. Y. Tang, Z. Y. Qin, W. Q. Liao, Z. S. Wang, J. J. Qin, X. G. Li, H. L. Wang, M. Gusain, F. C. Liu, Y. Y. Pan, M. S. Xu, J. Wang, R. Liu, C. F. Zhang, R. G. Xiong, W. E. I. Sha and Y. Q. Zhan, Highly Efficient 1D/3D Ferroelectric Perovskite Solar Cell, *Adv. Funct. Mater.*, 2021, **31**, 2100205.

19 A. Fakharuddin, M. K. Gangishetty, M. Abdi-Jalebi, S.-H. Chin, A. R. bin Mohd Yusoff, D. N. Congreve, W. Tress, F. Deschler, M. Vasilopoulou and H. J. Bolink, Perovskite light-emitting diodes, *Nat. Electron.*, 2022, **5**, 203–216.

20 R. Dong, Y. Fang, J. Chae, J. Dai, Z. Xiao, Q. Dong, Y. Yuan, A. Centrone, X. C. Zeng and J. Huang, High-Gain and Low-Driving-Voltage Photodetectors Based on Organolead Triiodide Perovskites, *Adv. Mater.*, 2015, **27**, 1912–1918.

21 H. Zhu, Y. Fu, F. Meng, X. Wu, Z. Gong, Q. Ding, M. V. Gustafsson, M. T. Trinh, S. Jin and X. Y. Zhu, Lead halide perovskite nanowire lasers with low lasing thresholds and high quality factors, *Nat. Mater.*, 2015, **14**, 636–642.

22 G. Kieslich, S. Sun and A. K. Cheetham, An extended Tolerance Factor approach for organic–inorganic perovskites, *Chem. Sci.*, 2015, **6**, 3430–3433.

23 G. Kieslich, S. Sun and A. K. Cheetham, Solid-state principles applied to organic–inorganic perovskites: new tricks for an old dog, *Chem. Sci.*, 2014, **5**, 4712–4715.

24 V. M. Goldschmidt, Die Gesetze der Krystallochemie, *Naturwissenschaften*, 1926, **14**, 477–485.

25 C. C. Stoumpos and M. G. Kanatzidis, The Renaissance of Halide Perovskites and Their Evolution as Emerging Semiconductors, *Acc. Chem. Res.*, 2015, **48**, 2791–2802.

26 M. a. Mączka, M. Ptak, A. Gągor, D. Stefańska, J. K. Zaręba and A. Sieradzki, Methylhydrazinium Lead Bromide: Noncentrosymmetric Three-Dimensional Perovskite with Exceptionally Large Framework Distortion and Green Photoluminescence, *Chem. Mater.*, 2020, **32**, 1667–1673.

27 M. Mączka, A. Gagor, J. K. Zaręba, D. Stefanska, M. Drozd, S. Balciunas, M. Šimėnas, J. Banys and A. Sieradzki, Three-Dimensional Perovskite Methylhydrazinium Lead Chloride with Two Polar Phases and Unusual Second-Harmonic Generation Bistability above Room Temperature, *Chem. Mater.*, 2020, **32**, 4072–4082.

28 M. Mączka, M. Ptak, A. Gągor, J. K. Zaręba, X. Liang, S. Balčiūnas, O. A. Semenikhin, O. I. Kucheriv, I. y. A. Gural'skiy, S. Shova, A. Walsh, J. r. Banys and M. Šimėnas, Phase Transitions, Dielectric Response, and Nonlinear Optical Properties of Aziridinium Lead Halide Perovskites, *Chem. Mater.*, 2023, **35**, 9725–9738.

29 H. R. Petrosova, O. I. Kucheriv, S. Shova and I. A. Gural'skiy, Aziridinium cation templating 3D lead halide hybrid perovskites, *Chem. Commun.*, 2022, **58**, 5745–5748.

30 B. Saparov and D. B. Mitzi, Organic-Inorganic Perovskites: Structural Versatility for Functional Materials Design, *Chem. Rev.*, 2016, **116**, 4558–4596.

31 C. Katan, N. Mercier and J. Even, Quantum and Dielectric Confinement Effects in Lower-Dimensional Hybrid Perovskite Semiconductors, *Chem. Rev.*, 2019, **119**, 3140–3192.

32 X. Li, J. M. Hoffman and M. G. Kanatzidis, The 2D Halide Perovskite Rulebook: How the Spacer Influences Everything from the Structure to Optoelectronic Device Efficiency, *Chem. Rev.*, 2021, **121**, 2230–2291.

33 C. C. Fan, C. D. Liu, B. D. Liang, T. Y. Ju, W. Wang, M. L. Jin, C. Y. Chai and W. Zhang, Chiral three-dimensional organic-inorganic lead iodide hybrid semiconductors, *Chem. Sci.*, 2024, **15**, 11374–11381.

34 J. Bai, H. Wang, J. Ma, Y. Zhao, H. Lu, Y. Zhang, S. Gull, T. Qiao, W. Qin, Y. Chen, L. Jiang, G. Long and Y. Wu, Wafer-Scale Patterning Integration of Chiral 3D Perovskite Single Crystals toward High-Performance Full-Stokes Polarimeter, *J. Am. Chem. Soc.*, 2024, **146**, 18771–18780.

35 X. T. Li, M. Kepenekian, L. D. Li, H. Dong, C. C. Stoumpos, R. Seshadri, C. Katan, P. J. Guo, J. Even and M. G. Kanatzidis, Tolerance Factor for Stabilizing 3D Hybrid Halide Perovskitoids Using Linear Diammonium Cations, *J. Am. Chem. Soc.*, 2022, **144**, 3902–3912.

36 C. C. Fan, B. D. Liang, C. D. Liu, C. Y. Chai, X. B. Han and W. Zhang, Stable organic lead iodides with three-dimensional crystallographic and electronic structures showing high photoresponse, *Inorg. Chem. Front.*, 2022, **9**, 6404–6411.

37 P. F. Fu, S. L. Hu, J. Tang and Z. W. Xiao, Material exploration via designing spatial arrangement of octahedral units: a case study of lead halide perovskites, *Front. Optoelectron.*, 2021, **14**, 252–259.

38 H. Y. Zhang, X. J. Song, H. Cheng, Y. L. Zeng, Y. Zhang, P. F. Li, W. Q. Liao and R. G. Xiong, A Three-Dimensional Lead Halide Perovskite-Related Ferroelectric, *J. Am. Chem. Soc.*, 2020, **142**, 4604–4608.

39 D. Umeyama, L. Leppert, B. A. Connor, M. A. Manumpil, J. B. Neaton and H. I. Karunadasa, Expanded Analogs of Three-Dimensional Lead-Halide Hybrid Perovskites, *Angew. Chem., Int. Ed.*, 2020, **59**, 19087–19094.

40 Y. Y. Tang, Y. H. Liu, H. Peng, B. B. Deng, T. T. Cheng and Y. T. Hu, Three-Dimensional Lead Bromide Hybrid Ferroelectric Realized by Lattice Expansion, *J. Am. Chem. Soc.*, 2020, **142**, 19698–19704.

41 X. T. Li, Y. H. He, M. Kepenekian, P. J. Guo, W. J. Ke, J. Even, C. Katan, C. C. Stoumpos, R. D. Schaller and M. G. Kanatzidis, Three-Dimensional Lead Iodide Perovskiteoid Hybrids with High X-ray Photoresponse, *J. Am. Chem. Soc.*, 2020, **142**, 6625–6637.

42 W. Wang, C. D. Liu, C. C. Fan and W. Zhang, Reversible Glass-Crystal Transition in a New Type of 2D Metal Halide Perovskites, *Adv. Funct. Mater.*, 2024, 2407143.

43 J. M. Hoffman, X. Che, S. Sidhik, X. Li, I. Hadar, J. C. Blancon, H. Yamaguchi, M. Kepenekian, C. Katan, J. Even, C. C. Stoumpos, A. D. Mohite and M. G. Kanatzidis, From 2D to 1D Electronic Dimensionality in Halide Perovskites with Stepped and

Flat Layers Using Propylammonium as a Spacer, *J. Am. Chem. Soc.*, 2019, **141**, 10661–10676.

44 L. Mao, P. Guo, M. Kepenekian, I. Hadar, C. Katan, J. Even, R. D. Schaller, C. C. Stoumpos and M. G. Kanatzidis, Structural Diversity in White-Light-Emitting Hybrid Lead Bromide Perovskites, *J. Am. Chem. Soc.*, 2018, **140**, 13078–13088.

45 T. Eickhoff, P. Grosse and W. Theiss, Diffuse reflectance spectroscopy of powders, *Vib. Spectrosc.*, 1990, **1**, 229–233.

46 C. Quarti, G. Grancini, E. Mosconi, P. Bruno, J. M. Ball, M. M. Lee, H. J. Snaith, A. Petrozza and F. D. Angelis, The Raman Spectrum of the $CH_3NH_3PbI_3$ Hybrid Perovskite: Interplay of Theory and Experiment, *J. Phys. Chem. Lett.*, 2014, **5**, 279–284.

47 M. Mączka, J. A. Zienkiewicz and M. Ptak, Comparative Studies of Phonon Properties of Three-Dimensional Hybrid Organic–Inorganic Perovskites Comprising Methylhydrazinium, Methylammonium, and Formamidinium Cations, *J. Phys. Chem. C*, 2022, **126**, 4048–4056.

48 M. Mączka, M. Ptak, K. Fedoruk, D. Stefańska, A. Gągor, J. K. Zaręba and A. Sieradzki, The lattice symmetrization worked, but with a plot twist: effects of methylhydrazinium doping of $MAPbI_3$ on phase transitions, cation dynamics and photoluminescence, *J. Mater. Chem. C*, 2024, **12**, 1396–1405.

49 K. Nakada, Y. Matsumoto, Y. Shimoi, K. Yamada and Y. Furukawa, Temperature-Dependent Evolution of Raman Spectra of Methylammonium Lead Halide Perovskites, $CH_3NH_3PbX_3$ (X = I, Br), *Molecules*, 2019, **24**, 626.